




## Open Archive Toulouse Archive Ouverte (OATAO)

OATAO is an open access repository that collects the work of Toulouse researchers and makes it freely available over the web where possible

This is an author's version published in: <http://oatao.univ-toulouse.fr/28773>

**Official URL:** <https://doi.org/10.1007/s11661-021-06396-1>

### **To cite this version:**

Slim, Mohamed Fares and Geandier, Guillaume and Malard, Benoît  and Rouillard, Fabien *Microstructural and Chemical Changes of a Ti-Stabilized Austenitic Stainless Steel After Exposure to Liquid Sodium at Temperatures Between 500 °C and 650 °C.* (2021) *Metallurgical and Materials Transactions A*, 52 (10). 4438-4453. ISSN 1073-5623

Any correspondence concerning this service should be sent to the repository administrator: [tech-oatao@listes-diff.inp-toulouse.fr](mailto:tech-oatao@listes-diff.inp-toulouse.fr)

# Microstructural and Chemical Changes of a Ti-Stabilized Austenitic Stainless Steel After Exposure to Liquid Sodium at Temperatures Between 500 °C and 650 °C

MOHAMED FARES SLIM, GUILLAUME GEANDIER, BENOIT MALARD, and FABIEN ROUILLARD

Ti-stabilized austenitic stainless steel was carburized in sodium containing a high carbon activity at three different temperatures, 500 °C, 600 °C, and 650 °C during 1000 hours and 5000 hours. The carbon profile, the carbide volume fraction, and the lattice parameter evolution as function of depth were determined using high-energy X-ray diffraction and electron probe microanalysis. At 650 °C and 600 °C, the carbon precipitated as  $M_{23}C_6$  and  $M_7C_3$  carbides in the sample. The volume fraction of  $M_7C_3$  carbides was lower than predicted by thermodynamic equilibrium using Thermo-Calc software<sup>®</sup>. At 500 °C, carbides almost did not form in the steel. Instead, high carbon supersaturation of the austenitic matrix occurred. Both results demonstrate that the carburization profile was strongly influenced by the kinetics of carbide formation at temperatures lower than 650 °C. High-energy X-ray diffraction measurements demonstrated that the austenite and carbide lattice parameters evolved along the carbon profile. Both measured lattice parameter profiles of austenite and  $M_{23}C_6$  carbide were compared to the ones predicted from chemical changes of austenite and carbides.

<https://doi.org/10.1007/s11661-021-06396-1>

## I. INTRODUCTION

IN the framework of the development of a new generation of sodium-cooled fast nuclear reactor (SFR), the French Alternative Energies and Atomic Energy Commission have launched a research program to optimize the control rod lifetime in reactor. The main objective of the control rod is to absorb neutrons to control the fission rate in the core of the reactor. In the current French SFR concept, the control rods are made of  $B_4C$  pellets encapsulated in stainless steel cladding. Sodium circulates inside and outside of the clads in normal operation. As part of the research program on control rods, a better understanding of the interaction between  $B_4C$  and the stainless steel cladding is needed.

Indeed, feedbacks from former French SFRs revealed that the lifetime of the control rods was limited by the embrittlement of the cladding induced by its interaction with  $B_4C$ . While past and recent studies made on the interaction of  $B_4C$  with stainless steel in sodium in out-of-pile conditions have revealed that the main corrosion process is the formation of a boride layer on the surface of stainless steel,<sup>[1-5]</sup> post-mortem analysis of stainless steel cladding after exposure in former French or English SFRs revealed the formation of a deep and highly carburized zone mainly.<sup>[6,7]</sup> Despite the fact that this corrosion discrepancy between in and out-of-pile condition is still not clearly understood, the formation of this carburization zone after exposure in nuclear reactor was clearly identified as the main cause of the cladding failure. The carburization of austenitic stainless steel at intermediate and high temperatures in liquid sodium and its effect on the mechanical properties were widely studied in the past.<sup>[8-23]</sup> It is well known that the mechanical properties (ductility, proof stress *etc.*) of steels are strongly modified after carburization.<sup>[11,15,24]</sup> The impact on the component mechanical behavior depends strongly not only on the carbon concentration profile (carburization depth and carbon concentration level) but also on all the modifications induced in the microstructure (volume fraction of carbides, composition of carbides, *etc.*). In order to better predict the clad

---

MOHAMED FARES SLIM and GUILLAUME GEANDIER are with the Université de Lorraine, CNRS, IJL, 54000, Nancy, France. Contact e mail: mohamedfaresslim@gmail.com, mohamed.fares.slim@esrf.fr BENOIT MALARD is with the CIRIMAT, Université de Toulouse, CNRS, INPT, UPS, ENSIACET 4, allée Émile Monso, 31030 Toulouse, France. FABIEN ROUILLARD is with the Université Paris Saclay, CEA, Service de la Corrosion et du Comportement des Matériaux dans leur Environnement, 91191, Gif sur Yvette, France.

lifetime, the carburization kinetics and a detailed description of all the microstructure modifications occurring during carburization of the stainless steel clad are clearly needed. First reports on the kinetics of microstructural and chemical changes of candidate clad stainless steels, 316L and, a titanium-stabilized austenitic stainless steel, AIM1\*, exposed in carburizing liquid

---

\*Austenitic Improved Material

---

sodium at temperatures between 500 °C and 650 °C for exposure times up to 5000 hours were determined from several complementary analysis techniques as optical microscopy (OM), high-energy X-ray diffraction (HEXRD), electron probe microanalyses (EPMA), and transmission electronic microscopy (TEM) analysis.<sup>[16,25,26]</sup> In that studies, the observed carburization profiles were compared to the ones predicted by diffusion-controlled transformations (DICTRA) software. In this paper, that work was reproduced on new samples of AIM1 stainless steel exposed in carburizing sodium between 500 °C and 650 °C for 1000 hours. Moreover, the evolution of the crystallographic parameters of the matrix and formed carbides were measured accurately along the carbon profile by HEXRD and compared to the ones predicted by the literature from the measured elementary composition of austenite and carbides at all temperatures.

## II. EXPERIMENTAL DETAILS

### A. Material and Carburization Experiments

The studied material was the titanium-stabilized austenitic stainless steel AIM1 quenched at 1130 °C and strain hardened during rolling to 25 pct. The detailed chemical composition of the studied steel is given in Table I. At initial state, the AIM1 alloy was composed of austenite and a small quantity of TiC carbide (about 1 to 2 wt pct). The grains were mostly equiaxed with an average size of 40  $\mu\text{m}$ .

AIM1 austenitic stainless steel samples were carburized at three different temperatures, 500 °C, 600 °C, and 650 °C for 1000 and 5000 hours. The carburization experiments were performed in a mild steel crucible (iron containing 0.38 wt pct of carbon) filled with around 2 liters of nuclear grade liquid sodium and containing additional mild steel plates. These mild steel plates were added in order to maintain a high carbon activity in sodium during the whole test duration. Before exposing to sodium, the AIM1 samples of dimensions  $20 \times 20 \times 1 \text{ mm}^3$  were cleaned in ethanol, and the liquid sodium was purified from dissolved oxygen using zirconium foil at 600 °C for three days (obtained oxygen concentration lower than 5 ppm). After carburization, the samples were cut and used for the different experimental characterizations. More details on the procedure for carburization experiments in sodium can be found in previous works.<sup>[16,17,25]</sup>

### B. High-Energy X-Ray Diffraction Experiment

The carburized samples were characterized by HEXRD in transmission mode at the Positron-Elektron-Tandem-Ring-Anlage (PETRA) P07-EH2 beamline (Deutsches Elektronen Synchrotron (DESY)-Petra III, Hamburg, Germany). A schematic presentation of the experimental set-up is given in Figure 1(a). The high-energy monochromatic rectangle-shaped beam with specific dimensions of 300  $\mu\text{m}$  in length and 2  $\mu\text{m}$  in height ( $E = 103.4 \text{ keV}$ ,  $\lambda = 0.119907 \text{ \AA}$ ) allowed working in transmission on the cross section of the sample of dimensions  $3 \times 3 \times 1 \text{ mm}^3$  (3 mm in the  $S_1$  and  $S_2$  directions and 1 mm in the  $S_3$  direction). The sample was animated by a translational movement along the  $S_3$  axis with a velocity  $V = 10 \mu\text{m/s}$ . A 2D Perkin Elmer detector ( $2048 \times 2048$  pixels, pixel size of  $200 \times 200 \mu\text{m}^2$ ) with a high acquisition rate (10 Hz) placed at 1.5 m from the sample was used to record the whole Debye-Scherrer rings with a maximum  $2\theta$  angle of 7.5°. The continuous translational movement of the sample coupled with the high image acquisition of the 2D detector allowed recording 2D images of a diffracted volume of  $300 \times 3000 \times 3 \mu\text{m}^3$  at every micrometer through all the traveled thickness (from the surface of the sample up to 500  $\mu\text{m}$  in depth). The size of the analyzed volume included a large number of metallic grains in order to be representative of the macroscopic carburization behavior of the sample. The beam alignment was made by a series of absorption and reflective scans, using the direct beam and a photodiode positioned behind the sample, in order to center the specimen and align the upper sample surface parallel to the beam. Considering the high photon energy and the resulting small scattering angles, the alignment had to be carried out at high precision thanks to three translations and rotations. The 2D detector sample distance and the detector tilts were calibrated using a cerium dioxide powder diffraction standard from the National Institute of Standards and Technology ( $\text{CeO}_2$ —Standard Reference Materials (SRM) 674b). The 2D diffraction images recorded during the experiments were integrated all around the rings using Python Tool for Fast Azimuthal Integration (PyFAI) software.<sup>[27]</sup> The obtained 1D diffractograms (Intensity vs  $2\theta$ ) were corrected from the instrumental aberration, using the powder diffraction standard, and analyzed with a full Rietveld refinement procedure using MAUD software (Material Analysis Using Diffraction).<sup>[28]</sup> After data processing, the Rietveld refinement allowed to determine the evolution of the mass fractions of the phases present in the alloy and their crystallographic parameters through the studied thickness. The experimental uncertainty was evaluated using a cerium dioxide powder diffraction standard ( $\text{CeO}_2$ —SRM 674b). The uncertainties on the measured mass fraction and lattice parameter were, respectively, 2 wt pct and 0.0005 Å. The carbides mass fractions determined by the previous Rietveld procedure allowed the calculation of the carbon concentration trapped in carbides using Eq. [1]:

**Table I. Composition of the AIM1 Austenitic Stainless Steel (wt pct) Analyzed by Inductively Coupled Plasma-Optical Emission Spectrometry (ICP-OES) and Combustion Analysis for Carbon**

| Cr    | Ni    | Mo   | C    | Ti   | Mn   | Co   | Si   | Cu   | Al    | Fe   |
|-------|-------|------|------|------|------|------|------|------|-------|------|
| 14.35 | 14.05 | 1.40 | 0.09 | 0.36 | 1.40 | 0.02 | 0.73 | 0.12 | 0.015 | Base |

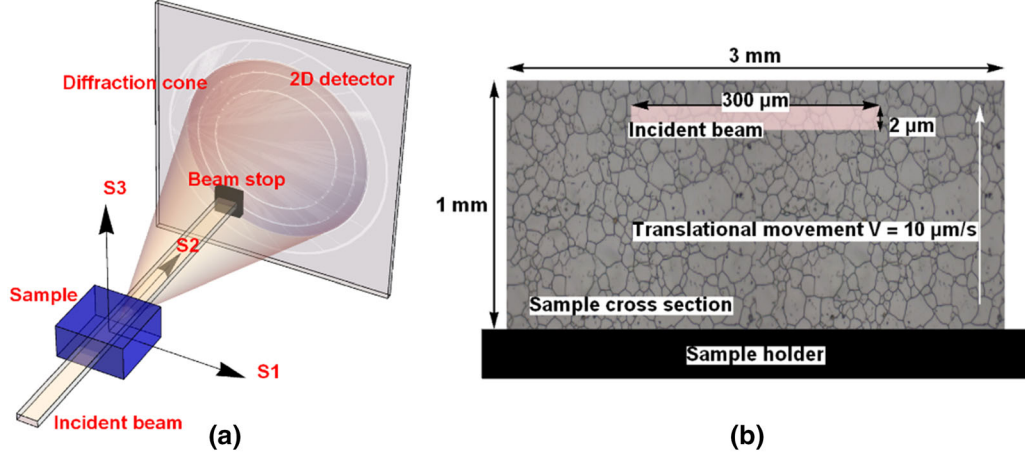


Fig. 1 (a) Experimental set up of the HEXRD measurements, (b) Schematic view of the sample cross section with the incident beam (not to scale).

$$w_C^{\text{Carbides}} (\text{wt pct}) = f^{M_{23}C_6} \cdot w_C^{M_{23}C_6} + f^{M_7C_3} \cdot w_C^{M_7C_3} + f^{TiC} \cdot w_C^{TiC}, \quad [1]$$

where  $f^X$  is the mass fraction of the phase X and  $w_C^X$  the carbon mass fraction in the phase X.

### C. Electron Probe Microanalysis Experiment

The carbon concentration profiles within the depth of the samples were measured using an SX 100 CAMECA EPMA operated at 15 kV and 20 nA using the phi-rho-z method. The analytical crystal for  $K_\alpha$  C was LPC2, and the carbon standard used for quantification was SiC. To get the best reliable carbon profiles with carbon contained both in substrate grains and grain boundaries, four surface profiles of  $2 \times 50 \mu\text{m}^2$  were averaged. The profiles were conducted up to mid-thickness of the sample, *i.e.*, 500  $\mu\text{m}$ . More details on the measurement procedure are available in previous works.<sup>[16,17,25]</sup>

### D. Transmission Electron Microscopy and Focused Ion Beam Thin Lamellas Preparation

Three thin lamellas were extracted parallel to the sample surface of AIM1 alloy carburized at 650 °C for 1000 hours at distances of 10, 100, and 300  $\mu\text{m}$  (along the  $S_3$  axis) from the surface by focus ion beam (FIB), using a scanning electron microscope-FIB FEI Helios NanoLab 600. One lamella was extracted from AIM1 alloy carburized at 600 °C for 1000 hours at distance of 100  $\mu\text{m}$ . The lamellas were investigated by TEM. JEOL

TEM microscope was operated at 200 kV (ARM FEG). TEM micrographs and STEM-EDX were made on the lamellas. The composition measurements were performed with a BRUKER XFlash EDXS Silicon Drift Detector.

## III. MODELING PROCEDURE

### A. Carburization Kinetics Modeling Using DICTRA

The carburization profiles of the AIM1 stainless steel at the experimental studied temperatures and exposure times were simulated using the DICTRA module (database MOBFE2) implemented in the Thermo-Calc software (database TCFE9). DICTRA has been used successfully to simulate carburization in multicomponent systems at high temperature (850 °C).<sup>[29-31]</sup> In this study, a one-dimension model based on the homogenization approach was used assuming that carbon diffusion occurred only in the matrix (faster diffusion through grain boundaries was not considered) and that no diffusion occurred through the carbides (thus, carbides were considered as diffusion obstacles for carbon). The labyrinth factor was kept constant for all simulations and equal to  $f^2$  as usually used in literature.<sup>[18,30-33]</sup> The labyrinth factor is implemented in DICTRA software and used to consider the influence of the presence of carbides on the carbon diffusion in the matrix. More details on the homogenization model implemented in the DICTRA module are available in the literature.<sup>[34,35]</sup> The geometrical model used in the simulations was a planar one-dimensional unit cell with



a length equal to the half sample thickness since carbon diffusion occurred uniformly from both sides of the sample (symmetry assumption). The phases authorized to form during the simulation were austenite and the two  $M_{23}C_6$  and  $M_7C_3$  carbides. TiC carbide was detected by HEXRD, but as its amount was very low and no evolution of its mass fraction was experimentally observed during carburization, it was excluded from the simulations. Similarly, no graphite neither cementite was identified in the alloy; thus, their formation was also prevented in the simulations. The carbon activity corresponding to the carbon concentration measured by EPMA at the surface of the sample was used as boundary condition at the sodium–metal interface. The assumption of the symmetry at the middle plane of the samples provided the second boundary condition of zero flux for all the elements. The composition of AIM1 alloy presented in Table I was used to define the system. The carbon profile and carbides mass fractions ( $M_{23}C_6$  and  $M_7C_3$  carbides) predicted in the steel after carburization were compared to the HEXRD and EPMA experimental results.

#### IV. THEORETICAL LATTICE PARAMETER ESTIMATION

The evolution of the austenite lattice parameter as a function of carbon and alloying elements concentrations was taken from literature. First, the lattice expansion coefficient relating the lattice parameter of austenite to the carbon contents varies between 0.028 and 0.054 Å / (wt pct) C in the literature.<sup>[36–44]</sup> In our study, an intermediate value of 0.041 Å / (wt pct) C was used. Second, the influence of the alloying elements on the lattice parameter of austenite was taken from the work of Dyson and Holmes<sup>[38]</sup> which was the only complete work found in the literature on this topic. The final relation used to determine the theoretical lattice parameter as a function of the carbon and alloying elements is presented by Eq. [2]. The uncertainty on the theoretical lattice parameter determined by Eq. [2] was calculated using the uncertainty propagation equation based on the methodology referenced in the metrology documents.<sup>[45,46]</sup>

$$a_\gamma = a_0 + 0.041(\pm 0.011) \text{ pct C}^\gamma + 0.00095(\pm 0.00015) \text{ pct Mn}^\gamma - 0.0002(\pm 0.00004) \text{ pct Ni}^\gamma + 0.0006(\pm 0.0003) \text{ pct Cr}^\gamma + 0.0056(\pm 0.0007) \text{ pct Al}^\gamma - 0.0004(\pm 0.0001) \text{ pct Co}^\gamma + 0.0015(\pm 0.0005) \text{ pct Cu}^\gamma + 0.0031(\pm 0.0004) \text{ pct Mo}^\gamma + 0.0039(\pm 0.0009) \text{ pct Ti}^\gamma, \quad [2]$$

where  $a_0$  is the lattice parameter at ambient temperature in the absence of carbon and alloying elements and  $\text{pctX}^\gamma$ , the wt pct of the element X in austenite as predicted by Thermo-Calc. The  $a_0$  value was obtained

by subtracting the lattice expansion caused by dissolved carbon and alloying elements in the as-received steel (given by Thermo-Calc at studied temperature) from the measured initial lattice parameter ( $a_\gamma^{\text{initial}}$ ) of AIM1 alloy. This last value was determined by HEXRD on a sample annealed in inert gas at 600 °C for 1000 hours in order to remove any residual stress induced by the sample processing (strain hardening mainly):  $a_\gamma^{\text{initial}} = 3.5890 \pm 0.0005$  Å. The lattice parameter ( $a_\gamma^{\text{initial}}$ ) was considered as a reference in our study.

Several experimental and theoretical studies have demonstrated the dependence of the  $M_{23}C_6$  (M = Cr, Fe, Mo) carbide lattice parameter on its metallic composition.<sup>[47–56]</sup> The data found in literature are presented in Figure 2.

The values of Yi *et al.*<sup>[52]</sup> were used to estimate the  $M_{23}C_6$  theoretical lattice parameter as a function of its metallic composition using the relation proposed in Eq. [3] because they cover all the composition range of  $M_{23}C_6$  carbides.

$$a^{M_{23}C_6} = w_{\text{Mo}}^{M_{23}C_6} \cdot a^{(\text{Mo,Cr})_{23}C_6} + w_{\text{Fe}}^{M_{23}C_6} \cdot a^{(\text{Fe,Cr})_{23}C_6} + \left(1 - w_{\text{Mo}}^{M_{23}C_6} - w_{\text{Fe}}^{M_{23}C_6}\right) \cdot a^{Cr_{23}C_6} \quad [3]$$

where  $w_X^{M_{23}C_6}$  is the mass fraction of the element X in the  $M_{23}C_6$  carbide,  $a^{(\text{X,Cr})_{23}C_6}$ , the lattice parameter from literature corresponding to the mass fraction of X in  $M_{23}C_6$  (see Figure 2), and  $a^{Cr_{23}C_6}$ , the  $Cr_{23}C_6$  lattice parameter.

The goal of this section was to predict a qualitative evolution of the austenite and  $M_{23}C_6$  carbide lattice parameters as a function of their composition. The predicted evolution was compared to the evolution measured by HEXRD in the results part.

#### V. RESULTS

##### A. AIM1 Carburized at 600 °C and 650 °C

###### 1. Microstructure

Figure 3 shows the cross-section images observed by OM on AIM1 alloy carburized at 600 °C and 650 °C for 1000 hours after chemical attack in oxalic acid. Three carburization zones were detected on both samples at both temperatures:

- First, near the sample surface, about 120  $\mu\text{m}$  thick and 210  $\mu\text{m}$  thick intragranular carburization zone was observed after exposure at 600 °C and 650 °C, respectively. In that zone, carbides formed at grain boundaries and within the substrate grains. The density of carbides in the substrate in that zone was very high as shown in Figure 4(b) after exposure at 650 °C. At grain boundaries, large globular carbides with a diameter about several hundredths of nanometer were observed. Acicular (needle shaped) and spheroidal carbides of about several tenths of nanometer were rather observed within the grains.

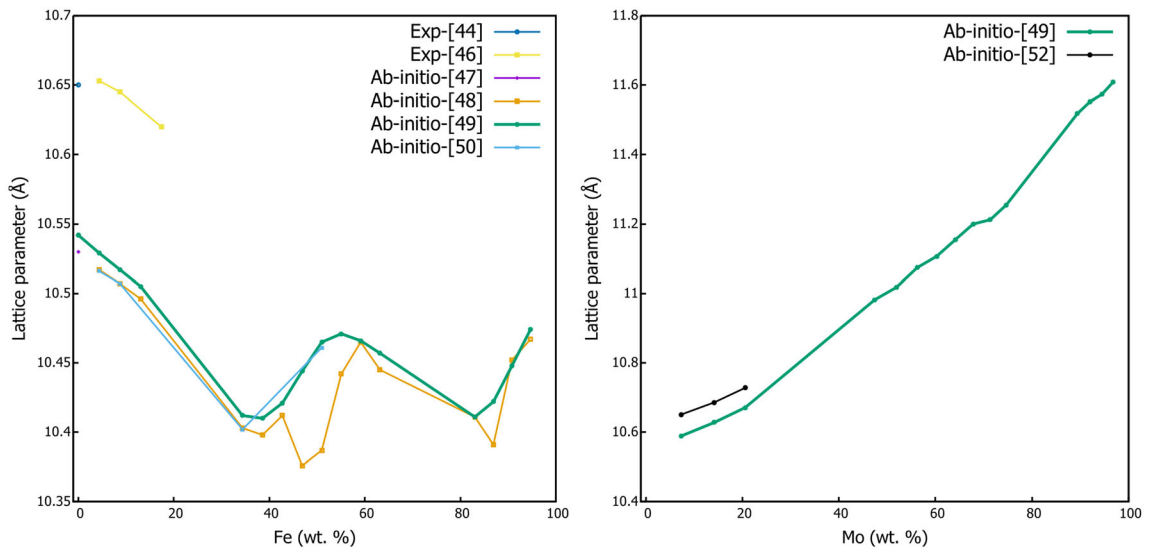


Fig. 2 Evolution of  $M_{23}C_6$  (M = Fe, Cr) or (M = Mo, Cr) lattice parameter as a function of Fe and Mo concentrations. Literature data obtained from experimental and ab initio calculation results.<sup>[47,49-55]</sup>

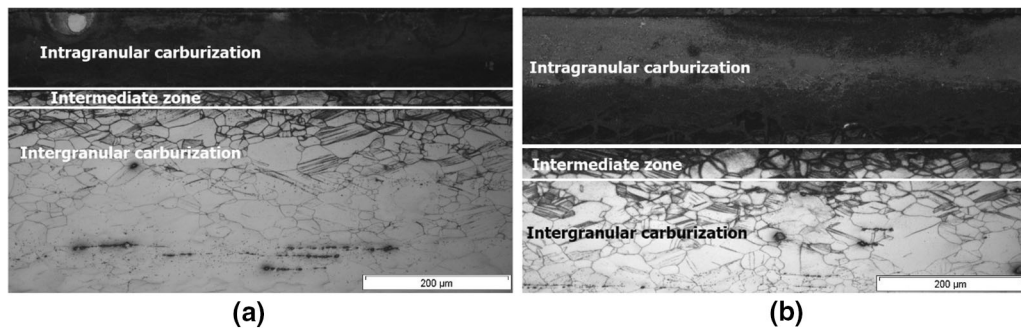


Fig. 3 Cross section image by OM of AIM1 alloy carburized at (a) 600 °C during 1000 h and (b) 650 °C during 1000 h.

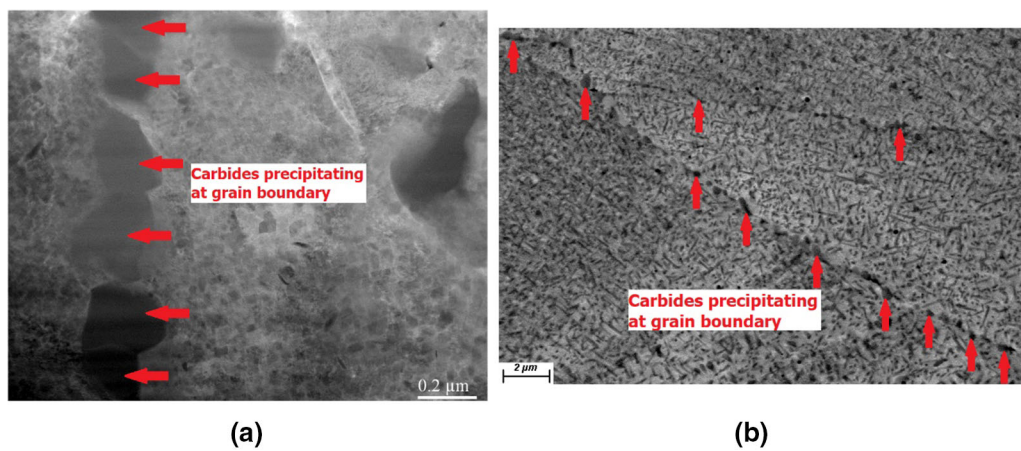


Fig. 4 (a) TEM annular dark field micrograph of the lamella extracted at 100 μm from the surface of AIM1 alloy carburized at 600 °C for 1000 h and (b) SEM cross section image at a distance of 20 μm from the surface of AIM1 alloy carburized at 650 °C for 1000 h.

– Then, an intermediate carburization zone was observed where carbides formed in the grain boundaries and in regions of the grains closed to grain boundaries. The proportion of the grain area where

a high density of carbides formed decreased with depth. This microstructure with a carbide density decreasing as the center of the substrate grain was approached revealed that carbide precipitation

occurred mainly *via* fast diffusion of carbon through grain boundaries then diffusion into the substrate grains.

- Deeper in the sample, carbides were only detectable in grain boundaries. This last zone formed the intergranular carburization zone.

## 2. Phases mass fractions

Figure 5 shows the evolution of austenite and carbides mass fractions in AIM1 alloy after carburization at 600 °C and 650 °C for 1000 hours measured by HEXRD. TiC carbides were initially present in the alloy before carburization and its mass fraction did not evolve at a detectable level for HEXRD after carburization.  $M_7C_3$  and  $M_{23}C_6$  carbides were mainly formed in the two samples.  $M_{23}C_6$  carbides are present in the whole thicknesses of the two samples with non-negligible quantity,  $\geq 2$  wt pct until 350  $\mu\text{m}$ . These carburization depths are in reasonable agreement with the carburized

zone depths determined from metallurgical attack (see Figure 3). In the sample carburized at 600 °C,  $M_7C_3$  carbides were only detected within the first 60  $\mu\text{m}$  below the sample surface. At 650 °C,  $M_7C_3$  carbides were detected up to a larger depth, 100  $\mu\text{m}$ . For both samples,  $M_{23}C_6$  carbides were formed through the whole sample thickness. The carburization level increased after longer exposure time: at 600 °C for 5000 hours, the maximum depth of  $M_7C_3$  carbides formation increased to 140  $\mu\text{m}$  and  $M_{23}C_6$  were detected in the whole sample with a mass fraction higher than 10 wt pct (not shown, see Reference 16).

## 3. Carbon concentration profile

Figure 6 shows a comparison between the carbon profile measured by EPMA and the carbon profile obtained using Eq. [1] from the Rietveld refinement of the HEXRD data for AIM1 alloys carburized at 650 °C and 600 °C for 1000 hours. Both profiles are in excellent agreement. Since Eq. [1] only considers the carbon

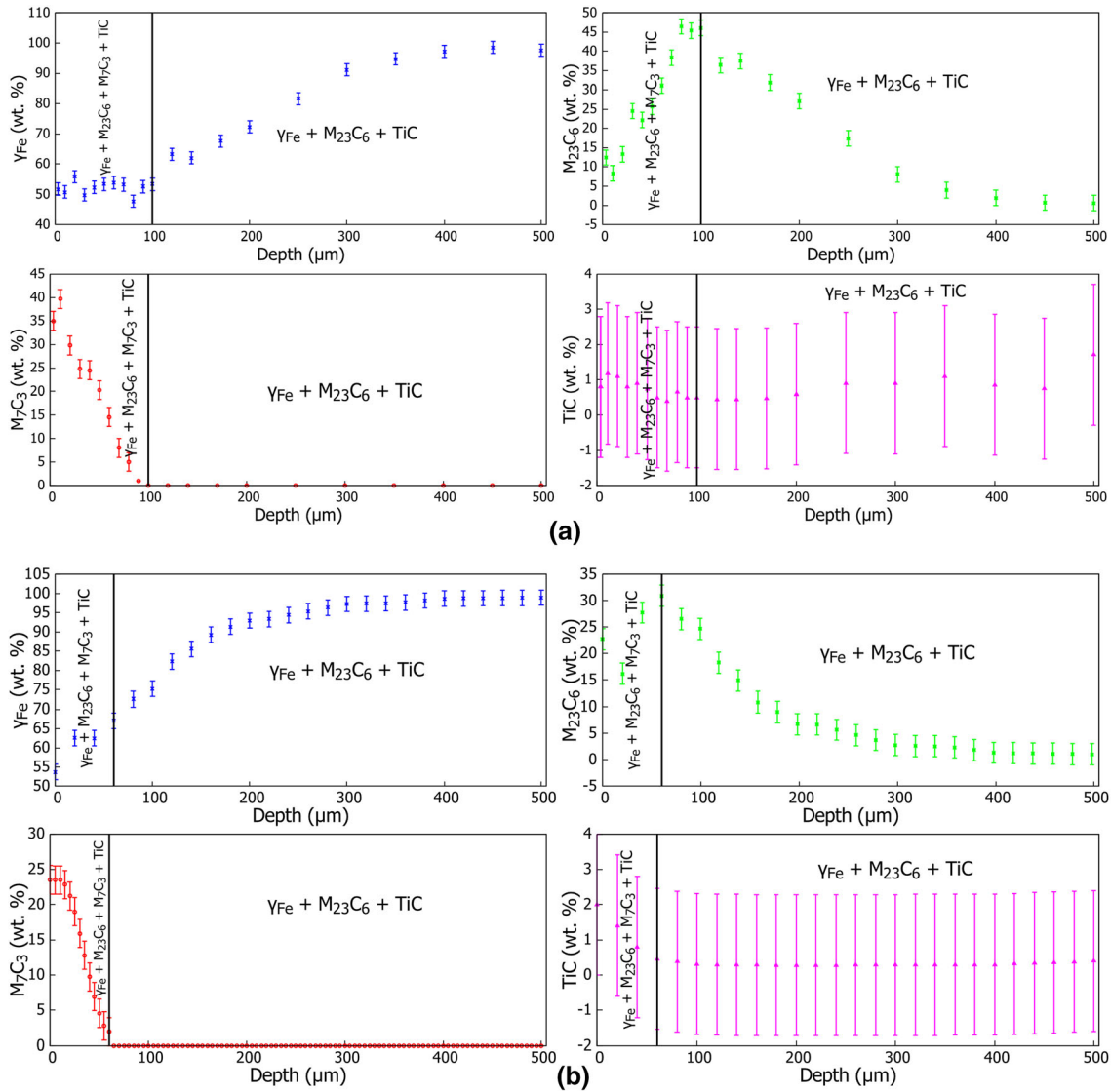


Fig. 5 Evolution of the austenite and carbides mass fractions in AIM1 alloy carburized at (a) 650 °C for 1000 h and (b) 600 °C for 1000 h.

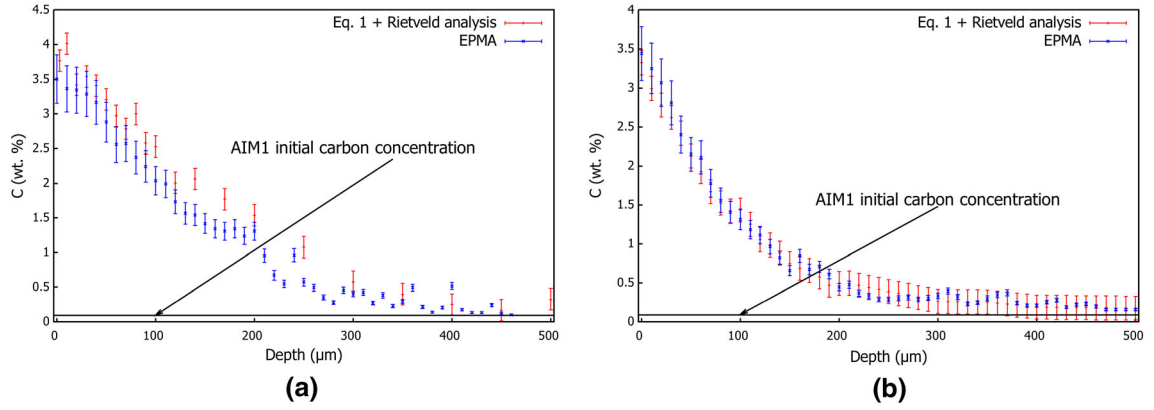


Fig. 6 Comparison between the carbon profiles determined by EPMA and using Eq. [1] with Rietveld analysis on HEXRD data of AIM1 carburized at (a) 650 °C for 1000 h and (b) 600 °C for 1000 h.

contained in carbides, this excellent agreement demonstrates that all carbon which diffused within the sample was trapped into carbides. This observation was justified with the low solubility of carbon in AIM1 (0.17 wt pct at the surface and 0.0003 wt pct in the core of the material, from DICTRA). A similar agreement was observed on the carbon concentration profiles of AIM1 carburized at 600 °C for 1000 hours (Figure 6(b)) and 5000 hours (not shown, see Reference 16). At 650 °C (respectively 600 °C), carbon enrichment was observed up to 350  $\mu\text{m}$  (respectively 300  $\mu\text{m}$ ) in depth. Then, the carbon concentration stabilized at a value slightly higher than the carbon concentration measured in the as-received steel.

#### 4. Chemical analysis

Quantitative STEM-EDX analysis of the compositions of  $\text{M}_{23}\text{C}_6$  carbides ( $\text{M} = \text{Cr, Fe, Mo, Ni}$ ) and austenite was carried out on two thin lamellas extracted from AIM1 carburized at 650 °C for 1000 hours (extracted at 100  $\mu\text{m}$  and 300  $\mu\text{m}$  from the sample surface). They are shown in Tables II and III. The chemical quantification of the matrix at 100  $\mu\text{m}$  and 300  $\mu\text{m}$  was carried out on almost equivalent regions, not far from carbide. The Cr/Fe and Mo/Fe concentration ratio in  $\text{M}_{23}\text{C}_6$  carbides increased with depth. The evolution of the composition of carbides combined with the evolution of the carbide density along the carbon profile induced a depth-dependent metallic elements depletion of austenite (Table III). The main evolution was observed on the concentration of Cr and Mo in austenite: it was much more depleted at 100  $\mu\text{m}$  in depth than at 300  $\mu\text{m}$  (see Table III). The Cr and Mo enrichments of  $\text{M}_{23}\text{C}_6$  were higher at 300  $\mu\text{m}$  than at 100

$\mu\text{m}$ . This higher Cr and Mo enrichment of  $\text{M}_{23}\text{C}_6$  carbides at 300  $\mu\text{m}$  did not result in higher Cr and Mo depletion of the matrix (see Table III). This was due to the smaller mass fraction of  $\text{M}_{23}\text{C}_6$  at 300  $\mu\text{m}$  (8 wt pct) compared to 100  $\mu\text{m}$  (46 wt pct).

#### 5. Thermodynamic and kinetic modeling of carburization

Figures 7(a-1, a-3, b-1, b-3) shows a comparison between the experimental measurements of the carbon profile and the carbides mass fractions and DICTRA simulations for AIM1 alloy carburized at 650 °C and 600 °C for 1000 hours. It is observed that the experimentally measured carburization depth was quite correctly predicted by DICTRA simulation. Nevertheless, the measured mass fraction of  $\text{M}_7\text{C}_3$  and  $\text{M}_{23}\text{C}_6$  carbides differed strongly from DICTRA predictions. In particular, DICTRA simulation predicted the formation of larger mass fraction of  $\text{M}_7\text{C}_3$  in the carburized zone for the two carburization temperatures. It predicted about 40–50 wt pct of  $\text{M}_7\text{C}_3$  at the sample surface and higher than 10 wt pct of  $\text{M}_7\text{C}_3$  at about 130  $\mu\text{m}$  in depth for the two temperatures (see Figures 7(a-1) and (b-1)). However, no  $\text{M}_7\text{C}_3$  was detected by HEXRD at depth higher than 60 and 100  $\mu\text{m}$  in the samples carburized at 600 °C and 650 °C, respectively. Moreover, the mass fractions of  $\text{M}_{23}\text{C}_6$  measured by HEXRD were much higher than predicted by DICTRA in the carburized zone at both temperatures. Thus, the  $\text{M}_{23}\text{C}_6/\text{M}_7\text{C}_3$  mass fraction ratio measured by HEXRD in the carburized zone was much larger than the one predicted by DICTRA.

From this observation, new DICTRA simulations were carried out rejecting the formation of  $\text{M}_7\text{C}_3$

Table II. Metallic Composition of  $\text{M}_{23}\text{C}_6$  ( $\text{M} = \text{Cr, Fe, Mo}$ ) in AIM1 Alloy Carburized at 650 °C for 1000 h

| Distance from the Sample Surface ( $\mu\text{m}$ ) | Fe (Wt Pct) | Cr (Wt Pct) | Mo (Wt Pct) | Ni (Wt Pct) |
|--|-------------|-------------|-------------|-------------|
| 100  | 52.21       | 38.41       | 3.17        | 4.08        |
| 300  | 22.36       | 62.17       | 10.64       | 1.40        |



**Table III. Composition of Austenite in AIM1 Alloy Carburized at 650 °C for 1000 h**

| Distance from the Sample Surface ( $\mu\text{m}$ ) | Fe (Wt Pct) | Cr (Wt Pct) | Mo (Wt Pct) | Ni (Wt Pct) |
|--|-------------|-------------|-------------|-------------|
| 100  | 74.27       | 2.30        | 0.01        | 20.87       |
| 300  | 69.00       | 14.00       | 1.10        | 15.12       |

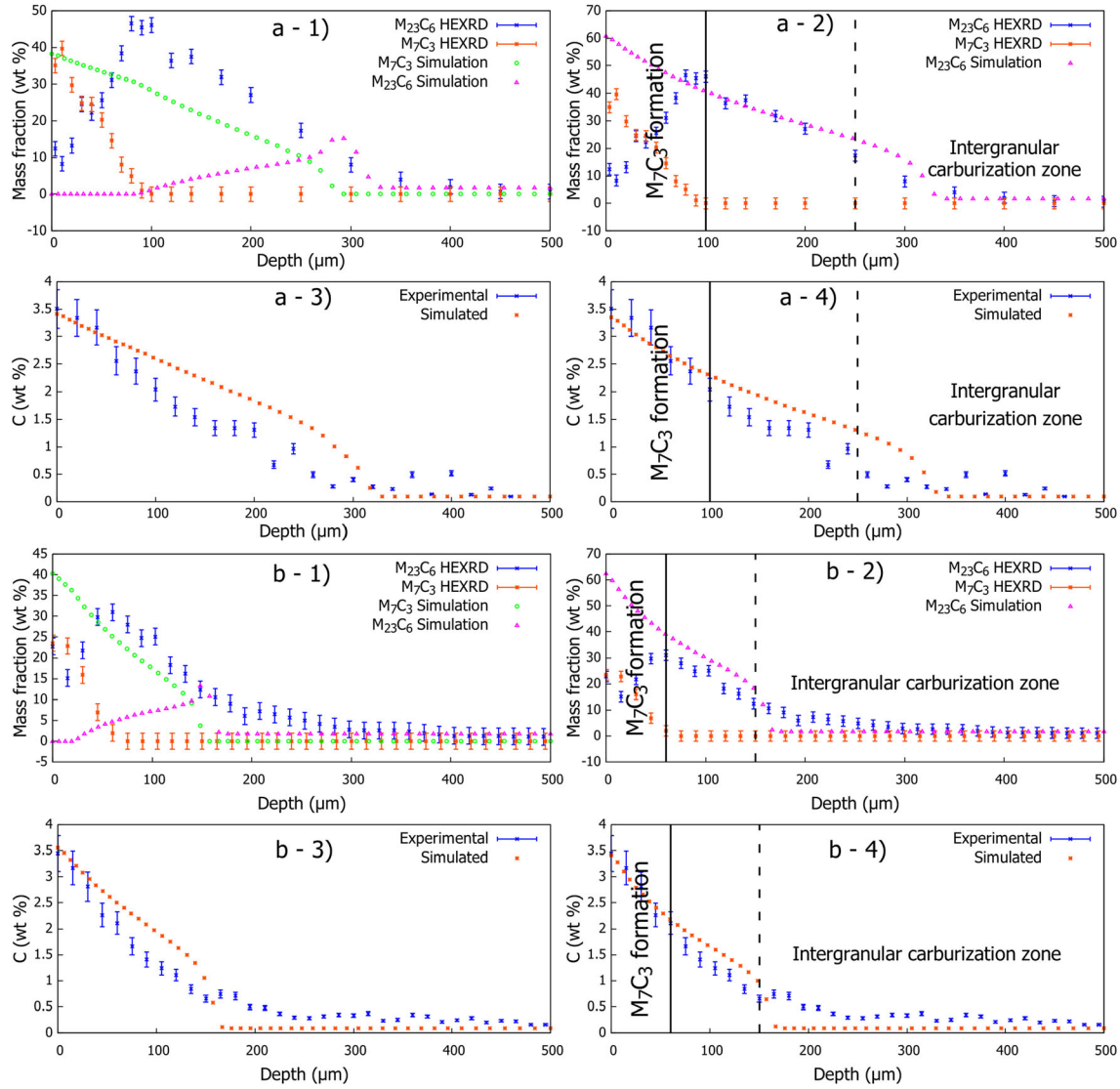


Fig. 7 Comparison between the experimental results and DICTRA simulations of the carbon profile and carbides mass fractions: (a 1, a 2, a 3, a 4) carburization at 650 °C for 1000 h, (b 1, b 2, b 3, b 4) carburization at 600 °C for 1000 h. Left column: simulation with  $\text{M}_7\text{C}_3$  formation. Right column: simulation rejecting  $\text{M}_7\text{C}_3$  formation.

carbide during carburization (see Figures 7(a-2, a-4, b-2, b-4)). With this assumption, DICTRA predicted correctly the carbon profile again and the  $\text{M}_{23}\text{C}_6$  mass fraction profile was quite in good agreement with the experimental observation, except in the nearest region to the surface where  $\text{M}_7\text{C}_3$  carbides formed. At 600 °C (see Figures 7(b-3, b-4)), the carbon profile tail observed experimentally from 150  $\mu\text{m}$  in depth was not predicted by the DICTRA simulation. This tail was due to the predominant diffusion of carbon through grain

boundaries forming, in consequence, the intergranular carburization zone (see Figure 3(a)). A better prediction of the carbon profile might be achieved using the grain boundary diffusion model implemented in DICTRA. Its use was out of the scope of the present work. Interestingly, the discrepancy between the measured carbon profile and the DICTRA carbon profile at the highest depths (around 350  $\mu\text{m}$ ) was lower at 650 °C than at 600 °C (Figures 7(a-3, a-4)). This result might be due to the

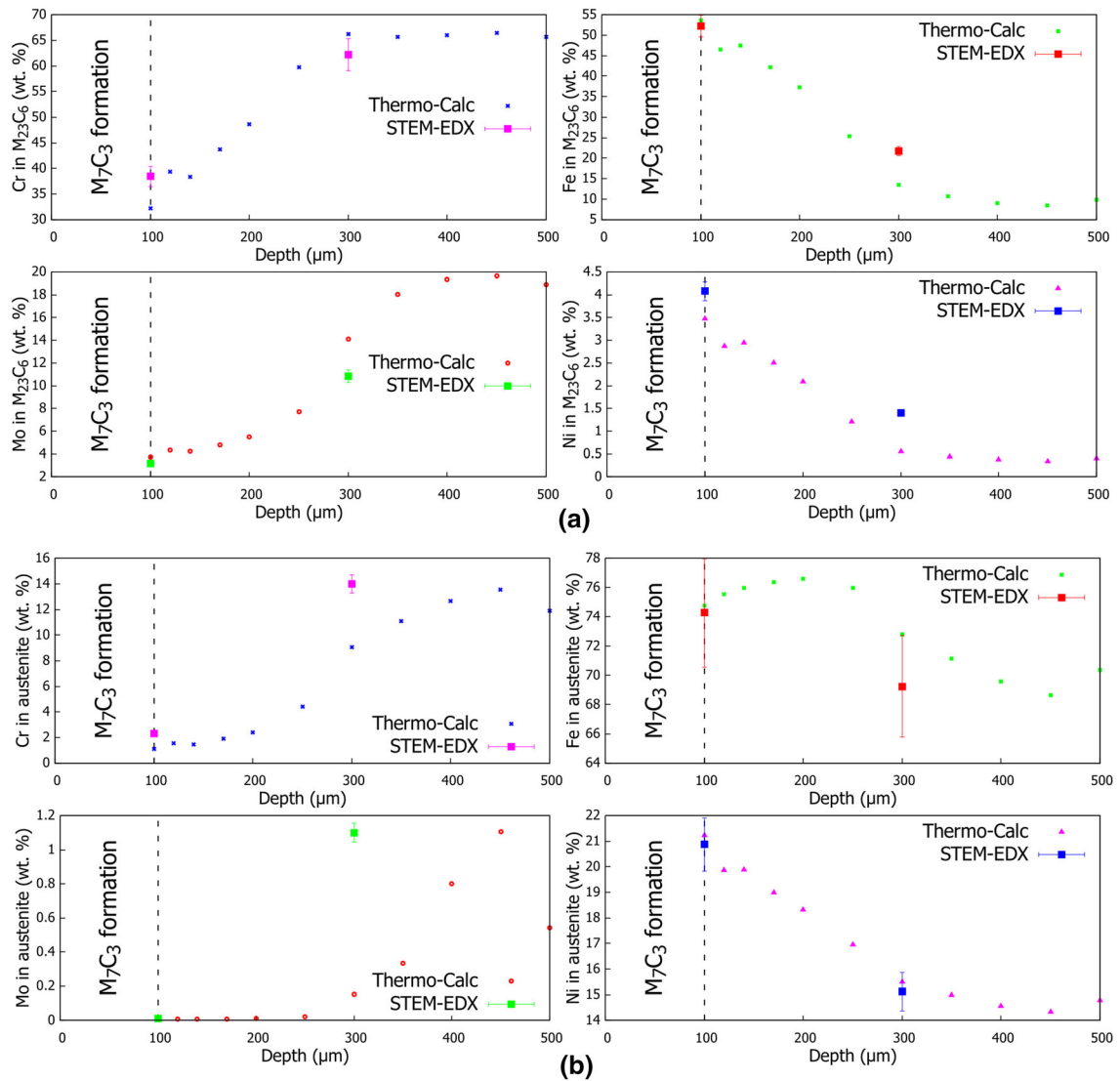


Fig. 8 Evolution of the composition, in AIM1 alloy carburized at 650 °C for 1000 h, predicted by Thermo Calc as a function of the sample depth: (a)  $M_{23}C_6$  and (b) austenite.

decreasing influence of grain boundary diffusion compared to bulk diffusion as the temperature increases.

The composition of carbides and austenite obtained after exposure at 650 °C for 1000 hours was predicted as a function of the total carbon concentration in the steel using Thermo-Calc. Since the transformation of  $M_{23}C_6$  into  $M_7C_3$  was not complete to reach thermodynamic equilibrium (see previously), the precipitation of the  $M_7C_3$  was banned in the Thermo-Calc calculations. In consequence, the compositions of carbides and austenite were only predicted for the regions where  $M_7C_3$  did not form that is to say from 100  $\mu\text{m}$  in depth. The compositions of  $M_{23}C_6$  and austenite shown in Tables II and III were compared with Thermo-Calc prediction in Figure 8. A quite good agreement between the measured composition and Thermo-Calc prediction was observed after carburization at 650 °C for 1000 hours. Thus, the  $M_{23}C_6$  and austenite compositions could be well described assuming local

thermodynamic equilibrium (without formation of  $M_7C_3$ ) at 650 °C.

From this important observation, the austenite and  $M_{23}C_6$  carbide theoretical lattice parameters obtained after 1000 hours at 650 °C were calculated from the composition predicted by Thermo-Calc calculations (see Section V-A-6). The same work was also done for austenite in AIM1 alloy carburized at 600 °C for 1000 hours (see Section V-A-6).

### 6. Lattice Parameter Evolution

Figure 9 shows a comparison between the austenite experimental lattice parameter in AIM1 alloy carburized at 650 °C and 600 °C for 1000 hours, determined *via* the Rietveld refinement of the HEXRD experiments data, and the austenite theoretical lattice parameter, calculated using Eq. [2] with the matrix composition determined by Thermo-Calc calculation from the experimental carbon profile (EPMA). The theoretical

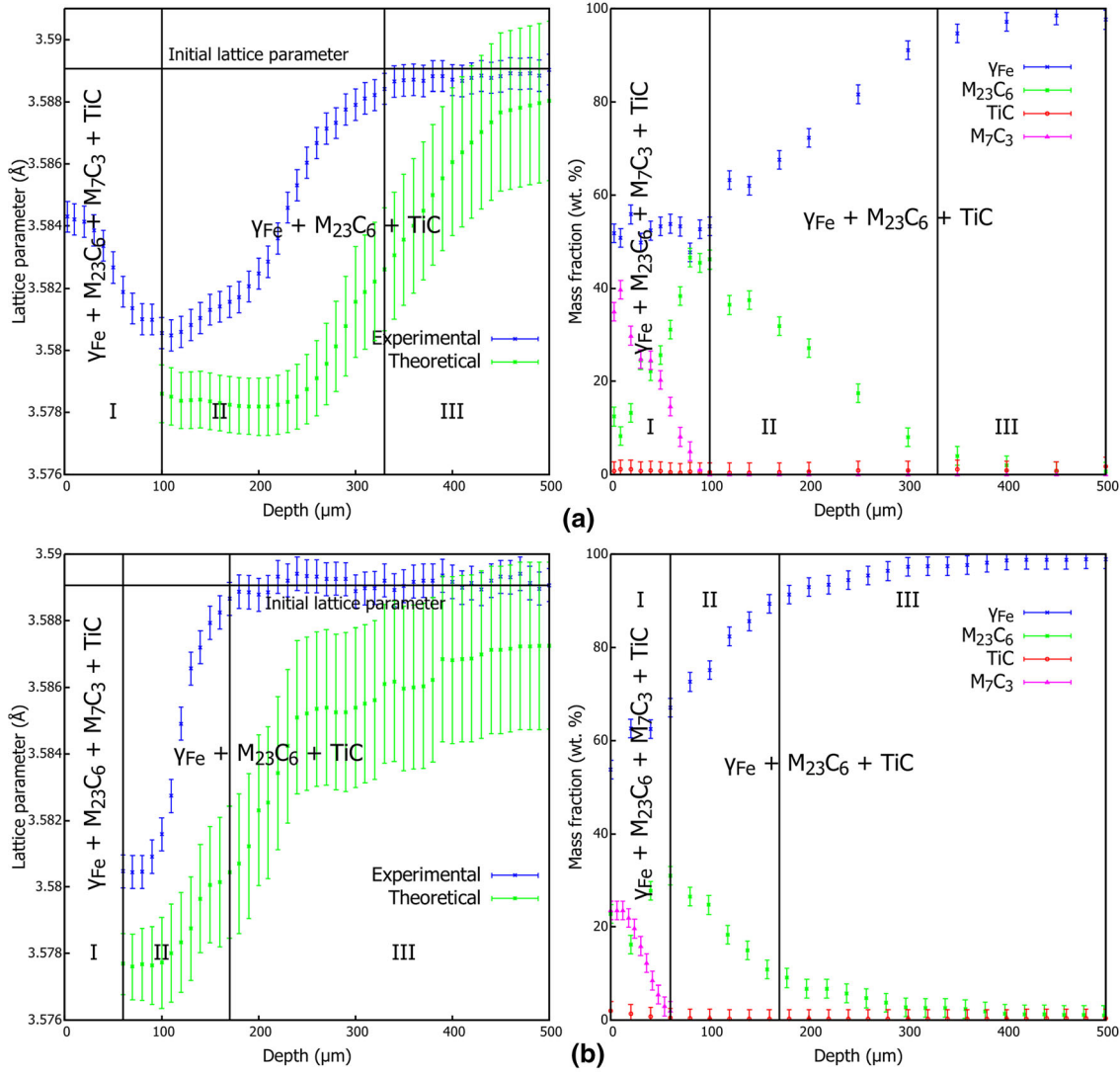


Fig. 9 Experimental and theoretical lattice parameters of the austenite and the mass fractions of the phases in AIM1 alloy carburized: (a) at 650 °C for 1000 h and (b) at 600 °C for 1000 h.

lattice parameter presents the same evolution as the experimental lattice parameter meaning that this evolution was mainly induced by the evolution of the austenite composition (mainly Cr and Mo). In this section, only the evolution of the experimental lattice parameter of AIM1 carburized at 650 °C for 1000 hours will be described. The evolution of the theoretical lattice parameter and the observed difference with the experimental lattice parameter will be discussed later. Figure 9 is divided into three zones:

- Zone I: This zone covered the first 100 μm near the surface. It corresponded to the zone where M<sub>23</sub>C<sub>6</sub> and M<sub>7</sub>C<sub>3</sub> precipitated. The austenite lattice parameter was lower than the initial lattice parameter before carburization. This was due to chromium and molybdenum depletion of austenite induced by carbide precipitation. The lattice parameter was maximal at the sample surface then decreased to

reach a minimum at 100 μm where the M<sub>23</sub>C<sub>6</sub> mass fraction was maximal.

- Zone II: This zone, from 100 μm to 330 μm in depth, was mainly composed of austenite and a decreasing mass fraction of M<sub>23</sub>C<sub>6</sub> carbides. The lattice parameter of austenite evolved on the opposite way of the mass fraction of M<sub>23</sub>C<sub>6</sub>: at the beginning of this zone, the M<sub>23</sub>C<sub>6</sub> mass fraction was maximal and the lattice parameter was minimal.
- Zone III: This zone started from 330 μm and corresponded to the intergranular carburization zone. It contained a small amount of M<sub>23</sub>C<sub>6</sub>. The lattice parameter of austenite was rather constant at a value roughly equal to the initial lattice parameter of the alloy before carburization.

The austenite lattice parameter in AIM1 carburized at 600 °C for 1000 hours (see Figure 9(b)) has the same evolution as AIM1 carburized at 650 °C for 1000 hours. In the same way, AIM1 carburized at 600 °C for

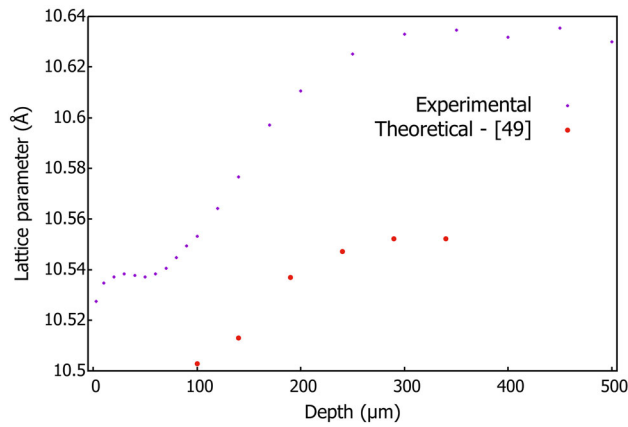


Fig. 10 Experimental and theoretical lattice parameters of the  $M_{23}C_6$  phase in the AIM1 carburized at 650 °C for 1000 h.

5000 hours have the same behavior except in Zone III where the experimental lattice parameter was lower than the as-received steel lattice parameter (not shown). It was due to a higher Cr and Mo depletion of the austenite matrix (due to precipitation of a higher amount of  $M_{23}C_6$  carbides).

Figure 10 shows a comparison between the  $M_{23}C_6$  experimental lattice parameter, determined *via* the Rietveld refinement of the HEXRD experiments data, and the  $M_{23}C_6$  theoretical lattice parameter, calculated using Eq. [3] and the composition of carbide determined by Thermo-Calc calculation from the experimental carbon concentration (EPMA). The lattice parameter of  $M_{23}C_6$  was minimal at the sample surface. Then, it increased with depth to reach a constant value from about 300  $\mu\text{m}$ . The theoretical lattice parameter, calculated using the data of Yi *et al.*,<sup>[52]</sup> showed a similar evolution but with lower values than the measured experimental lattice parameter. Again, the good agreement of the evolution of the simulated and measured  $M_{23}C_6$  experimental lattice parameter profiles indicates

that this parameter evolved mainly because of the evolution of the elementary composition of carbides. The same observations were done in the case of carburization at 600 °C for 1000 and 5000 hours (not shown).

## B. AIM1 Carburized at 500 °C

### 1. Phases mass fractions

The evolution of austenite and carbide mass fractions measured by HEXRD as function of sample depth for AIM1 alloy carburized at 500 °C for 1000 hours is showed in Figure 11. At this temperature and exposure time, only  $M_{23}C_6$  carbides were identified at the extreme surface of the sample (up to 6  $\mu\text{m}$  in depth). After 5000 hours, not presented here (see Reference 16),  $M_7C_3$  (up to 10  $\mu\text{m}$  in depth) and  $M_{23}C_6$  (up to 40  $\mu\text{m}$  in depth) were observed. A higher carbide density was observed in the alloy carburized for 5000 hours. At the sample surface, 25 wt pct of  $M_{23}C_6$  and 12 wt pct of  $M_7C_3$  were observed after 5000 hours whereas only 10 wt pct of  $M_{23}C_6$  was measured at the sample surface after 1000 hours (Figure 11).

### 2. Carbon concentration profile

Figure 12 shows a comparison between the carbon profile determined by EPMA and the carbon profile determined from the mass fraction of carbides detected by HEXRD (using Eq. [1]). The carbon concentration revealed by EPMA was much higher than the one calculated from the amount of formed  $M_{23}C_6$  carbides meaning that almost all carbon absorbed by the sample was not trapped into carbides. This result differed strongly from what was observed at 600 °C and 650 °C. The carbon concentration reached at any depth was much higher than the solubility limit of carbon at 500 °C given by Thermo-Calc (0.006 wt pct). In consequence, carbon supersaturation of the austenite matrix occurred. A similar behavior was observed on the sample

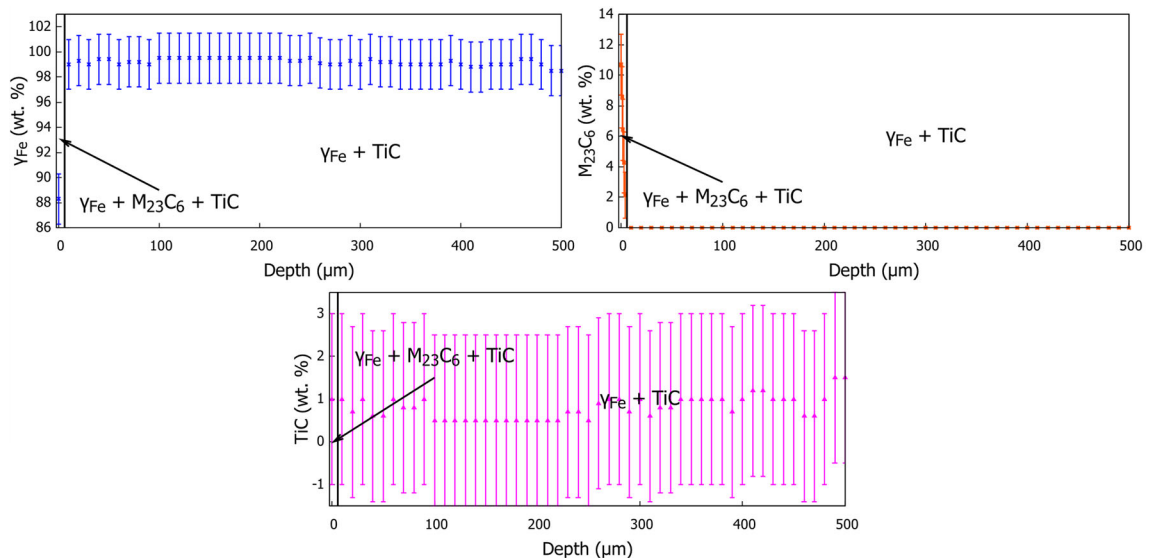


Fig. 11 Evolution of the phases mass fractions in AIM1 alloy carburized at 500 °C for 1000 h.



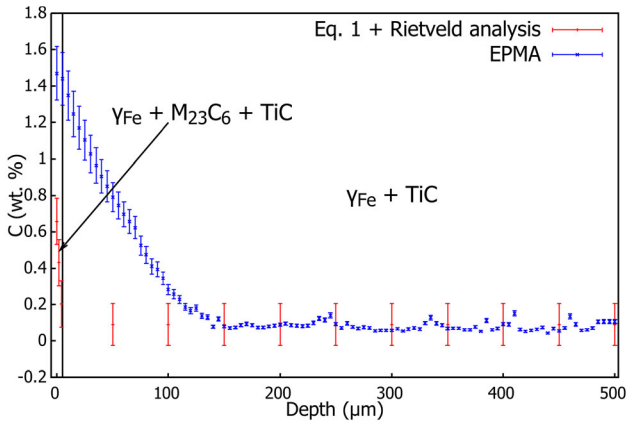


Fig. 12 Comparison between the carbon profiles determined by EPMA and using Eq. [1].

carburized at 500 °C for 5000 hours (not shown here, see Reference 16).

### 3. Lattice parameter evolution

In Figure 13, the evolution of the austenite experimental lattice parameter is compared, which determined via the Rietveld refinement of the HEXRD data and the austenite theoretical lattice parameter, calculated using Eq. [2] for AIM1 alloy carburized at 500 °C for 1000 hours. Since almost no carbides formed, only the evolution of carbon in austenite was taken into consideration for the calculation of the theoretical austenite lattice parameter (Eq. [2]). The evolution of the austenite lattice parameter in Figure 13 could be divided into three zones:

- Zone I: This is the zone where  $M_{23}C_6$  carbides were detected. The measured austenite lattice parameter is higher than the initial lattice parameter of non-carburized AIM1 alloy despite the formation of

- carbides (see results at 650 °C and 600 °C). The minimum value was reached at the surface then increased monotonously up to about 6  $\mu\text{m}$  in depth.
- Zone II: No carbides were detected in that zone. The experimental lattice parameter was higher than in Zone I and increased up to about 20  $\mu\text{m}$  in depth where it reached a maximum value. The evolution of the austenite lattice parameter in that region could not be explained by the evolution of the carbon concentration easily. Indeed, it evolved in the opposite way of the carbon concentration profile which was contrary of what was expected from Eq. [2].
- Zone III: In this last zone starting from about 20  $\mu\text{m}$  in depth, the austenite lattice parameter value decreased in agreement with the decrease of the carbon concentration (see Figure 12). An almost constant value was reached at the maximum depth of carbon enrichment, about 150  $\mu\text{m}$  from the sample surface (see Figure 12).

## VI. DISCUSSION

### A. Carburization at 600 °C and 650 °C

At 600 °C and 650 °C, almost all the carbon which diffused within the sample was trapped into  $M_{23}C_6$  and  $M_7C_3$  carbides in agreement with thermodynamic prediction. However, a strong disagreement between the measured and predicted  $M_{23}C_6$  and  $M_7C_3$  carbide mass fractions was observed (see Section V-A-5). The measured mass fraction of  $M_7C_3$  (respectively,  $M_{23}C_6$ ) was much lower (respectively higher) than the ones predicted by DICTRA simulations. These observations have been already reported by Romedenne *et al.* for carburization of 316L and AIM1 stainless steels at 600 °C.<sup>[16]</sup> This result strongly suggested that the carburization zone was not at local thermodynamic equilibrium. In particular,

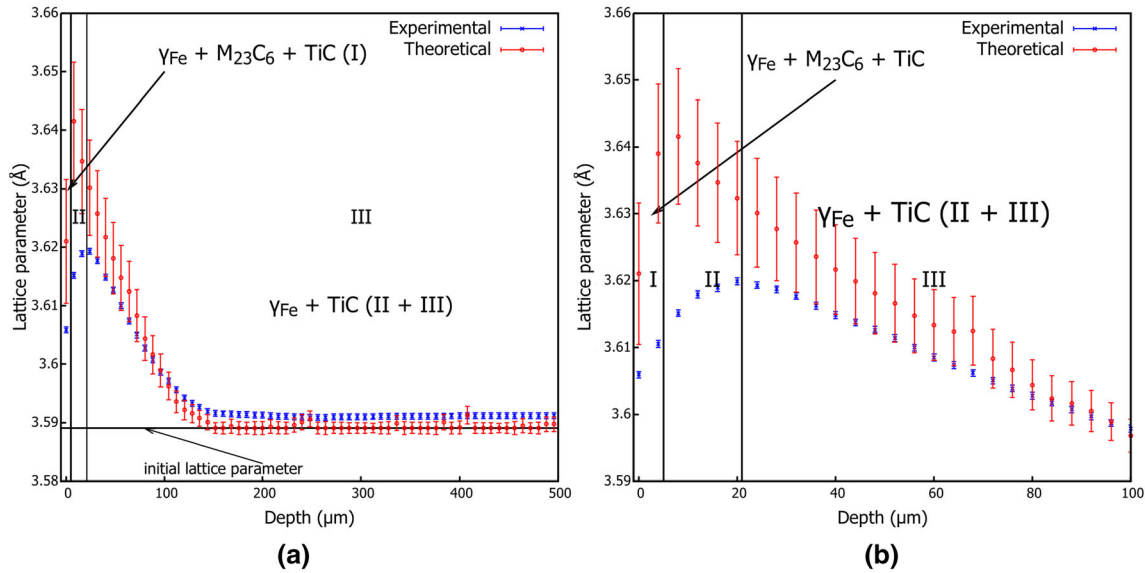


Fig. 13 (a) Experimental and theoretical lattice parameters of the austenite phase in the AIM1 alloy carburized at 500 °C during 1000 h, (b) Zoom in the first 100  $\mu\text{m}$  of depth.

the fraction of each carbide phases was very likely controlled by the slow rate of conversion of  $M_{23}C_6$  into  $M_7C_3$ . This slow conversion was already observed in other studies at 650 °C or higher temperatures.<sup>[57–59]</sup> Longer exposure time at 600 °C, 5000 hours, or higher temperature (650 °C instead of 600 °C) moved the proportions of  $M_7C_3$  and  $M_{23}C_6$  closer to the thermodynamic predictions but without reaching them. Despite this discrepancy with thermodynamic prediction for the carbide fractions, a rather good agreement could be observed between the measured and simulated (from DICTRA) carbon profiles. A better agreement could be found by rejecting the formation of  $M_7C_3$ , which was detected in low quantity in the steel, in the DICTRA modeling as already evidenced by Romedenne *et al.*<sup>[16]</sup>

For both temperatures, 600 °C and 650 °C, the highest amount of  $M_{23}C_6$  was observed at the depth where no more  $M_7C_3$  carbides were detected. The  $M_7C_3$  carbide started to form at almost the same carbon concentration,  $2 \pm 0.2$  wt pct, for the three carburized samples. From these observations, a scenario of carbides formation in relation to our experimental conditions can be drawn: as carbon diffused into the steel,  $M_{23}C_6$  carbides formed first, then, when reaching a carbon concentration of 2 wt pct,  $M_{23}C_6$  started to transform into  $M_7C_3$  carbide.

As a consequence of carbides precipitation, a modification of the composition of austenite in several alloying elements such as Cr and Mo mainly occurred (see Section V-A-4). This compositional modification has strong effect on the austenite lattice parameter value. In this study, it was evidenced that a part of the evolution of the measured austenite lattice parameter was reasonably well explained by the evolution of the composition of austenite, at least qualitatively. The evolution observed in the three zones identified in Figure 9(a) could be justified as followings starting with the deepest region:

- Zone III: In the region deeper than 400  $\mu\text{m}$ , a small amount of  $M_{23}C_6$  formed. As a consequence, a negligible quantity of Cr and Mo were trapped into carbides. Therefore, the austenite experimental lattice parameter was almost constant at a value roughly equal to the initial lattice parameter of the alloy before carburization. At about 400  $\mu\text{m}$ , a decrease of the theoretical lattice parameter was observed. This decrease was due to the increase of the  $M_{23}C_6$  mass fraction which resulted in a Cr and Mo depletion of austenite and consequently a decrease of the lattice parameter.
- Zone II: The lattice parameter evolution was directly related to the evolution of the  $M_{23}C_6$  mass fraction. The increase of the  $M_{23}C_6$  mass fraction resulted in the increase of Cr and Mo amounts trapped in carbides. By consequence, a higher Cr and Mo depletion in the matrix occurred. Thus, a decrease of the austenite experimental lattice parameter was observed such as predicted by Eq. [2].
- Zone I: The increase of the experimental austenite lattice parameter was due to the increase of  $M_7C_3$  mass fraction and the decrease of  $M_{23}C_6$  mass

fraction resulting from the  $M_{23}C_6 \rightarrow M_7C_3$  transformation. The decrease of the  $M_{23}C_6$  mass fraction and the increase of the  $M_7C_3$  mass fraction involve lower Cr and Mo depletion in the matrix as  $M_7C_3$  carbides are less Cr and Mo enriched compared to  $M_{23}C_6$  carbides. Therefore, the austenite experimental lattice parameter increased in this region.

The discrepancy between the theoretical and the experimental lattice parameter values can be explained by two factors: i) residual stress formed in the austenite phase due to the precipitation of carbides and ii) the coefficients used in Eq. [2] are not enough precise to describe quantitatively the lattice expansion of the AIM1 austenite cell.

A similar qualitatively good agreement between the evolution of the measured  $M_{23}C_6$  lattice parameter and its composition was observed. The  $M_{23}C_6$  lattice parameter evolved with the modification of its metallic composition as function of the carbon concentration in the steel. Hence, the increase of  $M_{23}C_6$  lattice parameter with depth was in good agreement with its enrichment in Cr and Mo (two atoms bigger than Fe) as the concentration of carbon decreased. The difference between the theoretical and experimental  $M_{23}C_6$  lattice parameter observed on Figure 10 can be due to different reasons again: i) the data used to estimate the  $M_{23}C_6$  theoretical lattice parameter were obtained by ab-initio calculation calculated at 0 K and were strongly dependent on the simulation parameters, ii) the estimation made using Eq. [2] cannot be considered as quantitative since it was simply based on a mixing law, or iii) residual stress formed.

## B. Carburization at 500 °C

At 500 °C, almost no carbides were formed and carbon supersaturation of austenite occurred. This phenomenon has been previously evidenced by different authors in highly carburizing gaseous environments on low alloyed steels and stainless steels in this range of temperatures (from 400 °C to 500 °C).<sup>[40,44,60–62]</sup> In that process, the carbon atoms dissolve massively in the octahedral interstices of austenite and do not form chromium-rich carbides because of the low mobility of the Cr atoms at this “low” temperature: expanded austenite forms. Expanded austenite is known to be metastable.<sup>[44,63]</sup> At long exposure times, stable austenite and chromium carbides are formed instead of expanded austenite.<sup>[44,63]</sup> This time- and temperature-dependent transformation could justify the higher density of  $M_{23}C_6$  and formation of  $M_7C_3$  in the sample carburized for longer exposure times (5000 hours instead of 1000 hours). This observation was in agreement with the results of Li *et al.*<sup>[64]</sup> who studied the thermal stability of expanded austenite at temperatures between 400 °C and 600 °C. They reported that expanded austenite decomposes into austenite and  $M_{23}C_6$  carbides by annealing at a temperature  $\geq 500$  °C for 20 hours.

At 500 °C,  $M_{23}C_6$  started to form at a carbon concentration equal to  $1.4 \pm 0.1$  wt pct for the two exposure times. For the longer exposure time,

5000 hours,  $M_7C_3$  started to form at the surface where carbon concentration is  $1.7 \pm 0.1$  wt pct. Based on the observations for the two exposure times, a scenario in relation with our experimental conditions can be drawn: the carbon which diffused within the sample dissolved first in the austenite lattice and formed expanded austenite. Then, when reaching a carbon concentration of 1.4 wt pct, the expanded austenite decomposed into expanded austenite (with a modified composition compared to the previous one) and  $M_{23}C_6$  carbides. Finally, when the carbon concentration is equal to 1.7 wt pct, the previous expanded austenite is decomposed into expanded austenite (more depleted in carbide and alloying elements),  $M_{23}C_6$ , and  $M_7C_3$  carbides.

The colossal carbon supersaturation of austenite caused an expansion of its lattice parameter (see Section V-B-3). The austenite lattice parameter evolution observed in Figure 13 could be explained as following from the deepest zone to the surface:

- Zone III: From the mid-thickness to 150  $\mu\text{m}$  in depth, the carbon concentration was constant and the value was equal to the initial concentration value in AIM1 (see Figure 12). In consequence, the austenite lattice parameter was almost constant also, as its evolution is related to the carbon profile. Then, at depth lower than 150  $\mu\text{m}$ , an increase of the carbon profile was observed (see Figure 12). In consequence, the lattice parameter increased.
- Zone II: A lower experimental lattice parameter than in the beginning of region III (at about 20  $\mu\text{m}$ ) was observed in this region despite the higher carbon concentration dissolved in austenite within region II (see Figure 12). This could be explained by the formation of a compressive residual stress gradient in the sample surface.<sup>[61,62,65-67]</sup>
- Zone I: Since  $M_{23}C_6$  carbides was observed in this zone, a part of the diffused carbon was trapped into carbides (see Section V-B-2). Therefore, the carbon concentration in austenite interstices decreased and resulted in a decrease of the austenite lattice parameter.

As in the case of carburization at 600 °C and 650 °C, the theoretical lattice parameter showed the same evolution as the experimental lattice parameter. Nevertheless, both curves were not in agreement quantitatively (see Figure 13). The discrepancy between the theoretical and the experimental lattice parameters can be explained by the same reasons as the ones proposed previously at higher temperature: formation of residual stresses or inaccurate coefficients used in Eq. [2].

## VII. CONCLUSIONS

The carburization behavior of AIM1 stainless steel exposed to highly carburizing liquid sodium at three different temperatures (500 °C, 600 °C, and 650 °C) and two exposure times (1000 and 5000 hours) was studied:

1. At carburization temperature  $\geq 600$  °C, almost all the carbon which diffused into the sample was trapped to form  $M_{23}C_6$  and  $M_7C_3$  carbides as predicted by Thermo-Calc software. However, the volume fraction of these two carbides did not obey the thermodynamic equilibrium prediction because of the low rate transformation of  $M_{23}C_6$  into  $M_7C_3$ . In consequence, the DICTRA simulations could predict properly the carbon profile and the  $M_{23}C_6$  mass fractions for temperatures  $\geq 600$  °C if  $M_7C_3$  precipitation was not allowed to form in the simulation.
2. At 500 °C, almost no carbides formed and carbon supersaturation of the austenitic matrix occurred. A low density of carbide was only observed at the extreme sample surface. Formation of carbide at this temperature was due to the long-time exposure and the metastable nature of the expanded austenite. The measured carbon profile was not predicted well by DICTRA.

It was evidenced that the austenite lattice parameter evolved along the carbon profile and that a non-negligible part of this evolution was chemically induced:

1. At temperatures  $\geq 600$  °C, a large part of this evolution was due to the depletion of chromium (and of molybdenum to a lower extent) induced by the formation of chromium-rich (and molybdenum) carbides.
2. At 500 °C, a large part of this evolution was due to the dissolution of carbon atoms in the octahedral interstices of austenite. The carbon supersaturation of the austenitic matrix resulted in the large expansion of the austenite lattice parameter.
3. The differences between the theoretical and experimental lattice parameters were very likely due to the formation of residual stress due to the volume change (Cr and Mo depletion of austenite and formation of carbides at temperatures  $\geq 600$  °C and austenite expansion at 500 °C). These residual stresses will be quantified in an upcoming paper.

## ACKNOWLEDGMENTS

The authors gratefully acknowledge the Deutsches Elektronen-Synchrotron (DESY-Petra III, Hamburg, Germany) for provision of beamtime at the PETRA P07-EH2 beamline. We would like to thank Olof Gutowski for assistance during the HEXRD experiments, A. Lequien and T. Vandenberghe for having carried out the EPMA analyses, P. Nerfie for the technical support in carrying out the carburizing tests, and J. Ghanbaja, S. Migot, and M. Emo from the Microscopies and Microprobes competence center of IJL for having carried out the TEM experiments. The RG4 project from CEA is thanked for having partially funded this study.



## FUNDING

This work was supported by the French Alternative Energies and Atomic Energy Commission, EDF, Framatome, the project CALIPSOoplus under the Grant Agreement 730872 from the EU Framework Programme for Research and Innovation HORIZON 2020 and the French State through the program “Investissements du futur” operated by the National Research Agency (ANR) and referenced by ANR-11-LABX-0008-01[68]

## CONFLICT OF INTEREST

On behalf of all authors, the corresponding author states that there is no conflict of interest.

## REFERENCES

1. M. Romedenne, F. Rouillard, D. Hamon, M. Tabarant, D. Monceau: 2019, Corrosion, vol. 75 (10), pp. 1173 82.
2. H.J. Heuvel, P. Holler, and P. Donner: *J. Nucl. Mater.*, 1985, vol. 130, pp. 517 23.
3. Ph. Dunner, H.J. Heuvel, and M. Horle: *J. Nucl. Mater.*, 1984, vol. 124, pp. 185 94.
4. R. E. Jr. Dahl, Boron carbide development for FFTF control elements (HEDL SA 565). United States.
5. K. Chandran, S. Anthonysamy, M. Lavanya, R. Sudha, P. R. Reshmi, D. Annie, R. Raja Madhavan, T. N. Prasanthi, C. Sudha, S. Saroja, V. Ganesan: *Procedia Engineering*, 2014, vol. 86, pp. 631 38.
6. F. Rouillard, M. Romedenne, Etat de l'art sur l'interaction B4C acier de gaine et loi de durée de vie des gaines des éléments absorbants NT DPC/SCCME 17 789 A 2017 (2017).
7. M.M. Oakden, B. Munro, J.E. Brocklehurst, and B.T. Kelly: *Fast Reactor Core Fuel Struct. Behav.*, 1990, vol. 4 (6), pp. 33 39.
8. W.F. Holcomb: *Nucl. Eng. Des*, 1967, vol. 6, pp. 264 72.
9. F.B. Litton and A.E. Morris: *J. Less Common Metals*, 1970, vol. 22, pp. 71 82.
10. W. J. Anderson, G. V. Sneesby: Atomic International Report NAASR 5289 (1960).
11. A. Thorley, C. Tyzack: British Nuclear Energy Society, Conference Proceedings, 1971.
12. A.W. Thorley, A. Blundell, and W.G. Murphy: *Liquid Metal Eng. Technol.*, 1984, vol. 154, pp. 197 206.
13. J.R. Gwyther, M.R. Hobbell, and A.J. Hooper: *Metals Technol.*, 1974, vol. 1 (1), pp. 406 11.
14. W. Charnock, J.E. Cordwell, J.R. Gwyther, M.R. Hobbell, P. Marshall, and I.R. McLaughlin: International conference on the physical metallurgy of reactor fuel *Elements*, 1975, vol. 8, pp. 37 46.
15. J.L. Krankota: *J. Eng. Mater. Technol.*, 1976, vol. 98 (1), pp. 9 16.
16. M. Romedenne, F. Rouillard, D. Hamon, B. Malard, and D. Monceau: *Corros. Sci.*, 2019, vol. 159, art. no. 108147.
17. M. Romedenne, F. Rouillard, B. Duprey, D. Hamon, M. Tabarant, and D. Monceau: *Oxidat. Metals*, 2017, vol. 87, pp. 643 53.
18. C. Sudha, N.S. Bharasi, R. Anand, H. Shaikh, R. Dayal, and M. Vijayalakshmi: *J. Nucl. Mater.*, 2010, vol. 402 (2), pp. 186 95.
19. N. Sivai Baharasi, K. Thyagarajan, H. Shaikh, M. Radhika, A. K. Balamurugan, S. Venugopal, A. Moitra, S. Kalavathy, S. Chandramouli, A. K. Tyagi, R. K. Dayal, K. K. Rajan: *Metall. Mater. Trans. A*, 2012, vol. 43 A, pp. 561 71.
20. N. Sivai Baharasi, M. G. Pujar, K. Thyagarajan, C. Mallika, U. Kamachi Mudali, A. Dhaul, M. Nandagopal, A. Moitra, S. Chandramouli, K. K. Rajan: *Metall. Mater. Trans. A*, 2015, vol. 46 A, pp. 6065 80.
21. N.S. Baharasi, M.G. Pujar, C.R. Das, J. Philip, K. Thyagarajan, S. Paneerselvi, A. Moitra, S. Chandramouli, V. Karki, and S. Kannan: *J. Nucl. Mater.*, 2019, vol. 516, pp. 84 99.
22. H.U. Borgstedt: *J. Nucl. Mater.*, 2003, vol. 317, pp. 160 66.
23. A. Pardo, M.C. Merino, A.E. Coy, F. Viejo, M. Carboneras, and R. Arrabal: *Acta Mater.*, 2007, vol. 55, pp. 2239 51.
24. F. Rouillard: Influence de la carburation sur le comportement mécanique des aciers: Données d'entrée pour la loi de durée de vie des gaines des Eléments Absorbants et Réflexions, NT DPC/SCCME 18 872 A (2017).
25. M. Romedenne, Etude de la carburation et de boruration d'aciers inoxydables en milieu sodium: interaction B4C gaine, Thèse de doctorat de l'Université de Toulouse (2018).
26. M.F. Slim, G. Geandier, M. Romedenne, F. Rouillard, and B. Malard: *Oxidat. Metals*, 2021, <https://doi.org/10.1007/s11085-021-10039-6>.
27. J. Kieffer and D. Karkoulis: *J. Phys.*, 2013, vol. 425, art. no. 202012.
28. L. Lutterotti, S. Matthies, H. R. Wenk: Proceeding of the 12th International Conference on Textures of Materials (ICOTOM 12), 1999, vol. 1, p. 1599.
29. A. Borgenstam, A. Engstrom, L. Hoglund, and J. Agren: *J. Phase Equilibria*, 2000, vol. 21 (3), pp. 269 80.
30. A. Engstrom, L. Hoglund, and J. Agren: *Metall. Mater. Trans. A*, 1994, vol. 25 (6), pp. 1127 34.
31. T. Turpin, J. Dulcy, and M. Gantois: *Metall. Mater. Trans. A*, 2005, vol. 36 (10), pp. 2751 60.
32. J. Garcia and O. Prat: *Appl. Surf. Sci.*, 2011, vol. 257 (21), pp. 8894 8900.
33. D. Rong, J. Gong, and Y. Jiang: *Procedia Eng.*, 2015, vol. 130, pp. 676 84.
34. H. Larsson, A. Engstrom: *Acta Mater.* 2006, vol. 54 (9), pp. 2431 39.
35. H. Larsson, L. Hoglund: *CALPHAD*, vol. 33 (3), pp. 495 501.
36. H. Kahn, G.M. Michal, F. Ernst, and A.H. Heuer: *Metall. Mater. Trans. A*, 2009, vol. 40A, pp. 1799 1804.
37. L. Cheng, A. Bottger, Th.H. de Keijser, and E.J. Mittemeijer: *Scripta Metall. Mater.*, 1990, vol. 24, pp. 509 14.
38. D.J. Dyson and B. Holmes: *J. Iron Steel Instit.*, 1970, vol. 208, pp. 469 74.
39. C.P. Scott and J. Drillet: *Scripta Mater.*, 2007, vol. 56, pp. 489 92.
40. Y. Sun, X. Li, and T. Bell: *Mater. Sci. Technol.*, 1999, vol. 15, pp. 1171 78.
41. T.S. Hummelshoj, T.L. Christiansen, and M.A.J. Somers: *Scripta Mater.*, 2010, vol. 63, pp. 761 63.
42. N.H. van Dijk, A.M. Butt, L. Zhao, J. Sietsma, S.E. Offerman, J.P. Wright, and S. van der Zwaag: *Acta Mater.*, 2005, vol. 53, pp. 5439 47.
43. S.J. Lee and Y.K. Lee: *Scripta Mater.*, 2005, vol. 52, pp. 973 976.
44. Y. Cao, F. Ernest, and G.M. Michal: *Acta Mater.*, 2003, vol. 51, pp. 4171 81.
45. JCGM 100: Evaluation of measurement data Guide to the expression of uncertainty in measurement (2008). <https://www.bipm.org/en/about-us/>.
46. JCGM 200: International vocabulary of metrology Basic and general concepts and associated terms (VIM) (2012). <https://www.bipm.org/en/about-us/>.
47. A.L. Bowman, G.P. Arnold, E.K. Storms, and N.G. Nereson: *Acta Crystallogr. B*, 1972, vol. B28, pp. 3102 03.
48. J.Y. Xie, N.X. Chen, L.D. Teng, and S. Seetharaman: *Acta Mater.*, 2005, vol. 53, pp. 5305 12.
49. P. Villars, L. D. Calvert: *Metals Park (OH): ASM* (1991).
50. C. Jiang: *Appl. Phys. Lett.*, 2008, vol. 92, art. no. 041909.
51. C.M. Fang, M.A. Van Huis, and M.H.F. Sluiter: *Acta Mater.*, 2016, vol. 103, pp. 273 79.
52. Y. Yijie, X. Weiwei, X. Fangfang, G. Tieqiang, and C. Lijie: *Adv. Eng. Res.*, 2017, vol. 121, pp. 74 80.
53. J. Han, C. Wang, X. Liu, Y. Wang, Z. K. Liu: *J. Phys.*, 2012, vol. 24 (50), pp. 505503.
54. C. Fang, M. Van Huis, M. Sluiter, and H. Zandbergen: *Acta Mater.*, 2010, vol. 58 (8), pp. 2968 77.
55. Z.Q. Lv, F. Dong, Z.A. Zhou, G.F. Jin, S.H. Sun, and W.T. Fu: *J. Alloys Compd.*, 2014, vol. 607, pp. 207 14.
56. X. Gong, C. Cui, Q. Yu, W. Wang, W.W. Xu, and L. Chen: *J. Alloys Compd.*, 2020, vol. 824, art. no. 153948.
57. Y. Gong, D.J. Young, C. Atkinson, T. Olszewski, W.J. Quadackers, and R.C. Reed: *Corros. Sci.*, 2020, vol. 173, art. no. 108699.



58. H.J. Christ: *Mater. Corros.*, 1998, vol. 49 (4), pp. 258–65.
59. S. I. Ford, P. Munroe, D. Young: *John Stringer Symposium on High Temperature Corrosion*, 2001, pp. 77–85.
60. F. Ernst, Y. Cao, and G.M. Michal: *Acta Mater.*, 2004, vol. 52, pp. 1469–77.
61. T. Christiansen, M. A. J. Somers: *Metall. Mater. Trans. A*, 2009, vol. 40 A, pp. 1791–98.
62. T.L. Christiansen, T.S. Hummelshoj, and M.A.J. Somers: *Surf. Eng.*, 2010, vol. 26, pp. 242–47.
63. F. Ernst, Y. Cao, G.M. Michal, and A.H. Heuer: *Acta Mater.*, 2007, vol. 55, pp. 1895–1906.
64. X.Y. Li, S. Thaiwatthana, H. Dong, and T. Bell: *Surf. Eng.*, 2002, vol. 18 (6), pp. 448–52.
65. Y. Peng, Z. Liu, Y. Jiang, B. Wang, J. Gong, and M.A.J. Somers: *Scripta Mater*, 2018, vol. 157, pp. 106–09.
66. S. Jegou, T.L. Christiansen, M. Klaus, Ch. Genzel, and M.A.J. Somers: *Thin Solid Films*, 2013, vol. 530, pp. 71–76.
67. F.A.P. Fernandes, T.L. Christiansen, G. Winter, and M.A.J. Somers: *Acta Mater.*, 2015, vol. 94, pp. 271–80.
68. LabEx DAMAS: [labex.damas.univ-lorraine.fr](http://labex.damas.univ-lorraine.fr).

**Publisher's Note** Springer Nature remains neutral with regard to jurisdictional claims in published maps and institutional affiliations.